Ab initio calculations of the rate of carrier trapping and release at dopant sites in NaI: Tl beyond the harmonic approximation

Micah P. Prange [1,*] Niranjan Govind [2] and Sebastien N. Kerisit [1]

[1]*Physical Sciences Division, Physical and Computational Sciences Directorate, Pacific Northwest National Laboratory, Richland, Washington 99354, USA*

[2]*Environmental Molecular Sciences Division, Earth and Biological Sciences Directorate, Pacific Northwest National Laboratory, Richland, Washington 99354, USA*

(Received 11 July 2019; revised manuscript received 21 October 2019; published 13 January 2020)

We present *ab initio* calculations of electron capture and release coefficients as a function of temperature for Tl dopants in the widely used scintillator NaI, which is a soft ionic crystal. The modeled capture and release events occur by transitions mediated by multiple phonon absorption and emission between states with significantly different local geometries around the trapping site. We demonstrate that such transitions are not well-described by the normal harmonic approximation to the nuclear dynamics. We go beyond the harmonic approximation by numerically solving the vibrational Schrödinger equation for the motion along/of a single effective phonon coordinate. The localized trapped state is not correctly described by semilocal density functionals, so we employ a global hybrid functional tuned to reproduce the band gap and lattice constant of the host material. Our calculations, which combine plane-wave and embedded cluster electronic structure methods are in reasonable agreement with available experimental data for detrapping and predict an unusual temperature dependence for trapping rates.

DOI: 10.1103/PhysRevB.101.024304

I. INTRODUCTION

Thallium-doped sodium iodide (NaI:Tl) is the most used inorganic scintillator material [1] with a long history of many important applications [2]. The alkali halide salts exhibit large electron-phonon interaction and correspondingly interesting optical properties that have attracted a long history of study by laser spectroscopy [3–13]. In the past decade, demand for improved γ-ray detection systems has driven renewed interest in the scintillation mechanisms in alkali halide and related material systems [14–36]. Despite this considerable history of research, there are still many open questions regarding the complicated sequence of events following γ excitation, which involves many excitations coupling defects, lattice deformations, and electronic excitations.

A scintillator emits optical light after ionizing radiation deposits energy in the crystal, resulting in one to several highly energetic electrons and matching holes. These primary excitations in turn create secondary electrons and holes in an energy cascade. The timing and amount of emitted light are determined by the radiative recombination of these excitations—each recombination emits an optical photon. The energy of the original ionizing radiation quantum (γ ray, electron, α particle, etc.) is then inferred from the total amount (time-integrated intensity) of emitted light. Hence the response time, brightness, and ultimate energy resolution achievable in radiation detectors based on scintillation are determined by the dynamics of electron-hole recombination. Quantitative models of scintillation, therefore, need to account for the processes that determine the likelihood and timescales of radiative recombination. These quantities are determined by the collective motion of the electrons and holes, including self-trapping and trapping, and release from activators. Progress has been made recently, driven by improved time-resolved optical spectroscopy, in the development of microscopic models of radiation transport following γ excitation. This research has increased knowledge of the photophysics to the point of quantitative knowledge of the types and populations of different excitation species, including electronically excited activators (impurities) [37], charged and neutral self-trapped electronic excitations [26], and free electron-hole pairs [18,20,38] in a few systems.

In this work we examine the case of a Tl activator in a NaI crystal. In the ground state, Tl exists in a +1 charge state as an isovalent substituent of Na in the NaI rocksalt structure. After γ excitation, the Tl^+ sites can trap both holes ($Tl^+ + h^+ \rightarrow Tl^{++}$) and electrons ($Tl^+ + e^- \rightarrow Tl^0$). Tl^+ can also trap neutral triplet excitons, resulting in an excited species we label Tl^* that decays radiatively producing the scintillation light. Tl^* can also be formed by sequential trapping of carriers of opposite sign (e.g., $Tl^0 + h^+ \rightarrow Tl^*$). This knowledge comes from a long history of models posited initially to explain the observed optical properties of self-trapped holes [4–7]. These models were later extended in an effort to quantitatively describe the fundamental limits imposed on radiation detection systems by intrinsic properties of the scintillating crystal [16,18,23,26,33]. Insights gained from these models and other theoretical work [37,39–41]

*Author to whom all correspondence should be addressed: micah.prange@pnnl.gov

include the realization that carrier trapping plays a key role in many aspects of scintillation, including limiting the achievable energy resolution for high-energy γ-ray spectroscopy. Understanding carrier trapping dynamics is also a prerequisite for cogent material design. For example, much effort has been expended trying to improve scintillator performance by codoping [42–50]. To date, these efforts have been largely empirical since a lack of detailed knowledge of the relative trapping rates at different dopant sites precludes the development of serious working hypotheses regarding the mechanisms by which performance might be improved by the introduction of new traps. Holes quickly self-trap in alkali halides [9] if they do not trap on activators. Afterward, they move diffusively. Electrons, on the other hand, do not self-trap in NaI. Instead, they travel ballistically away from the ionization track until they are drawn back by electrostatic attraction to the positively charged track core. To participate in luminescence, these electrons must end up at an activator site along with a hole. Competition between different types of traps, therefore, determines the population of electrons available for radiative recombination. Hence, the electron trapping (and release) dynamics represent a key source of uncertainty in the current generation of scintillation models. This work is an attempt to fill this knowledge gap using electronic structure calculations. Recent work using thermally stimulated luminescence [51] provides some experimental data regarding electron release from Tl in NaI:Tl. For these reasons, we have chosen to study electron trapping and detrapping from Tl sites in NaI:Tl theoretically. We do this by using and extending electronic structure approaches to inelastic electron scattering by phonons [52,53] to simulate the vibrational dynamics around Tl in NaI:Tl and the probability that these vibrations cause an electron to be trapped or released by multiphonon processes.

II. THEORETICAL FRAMEWORK AND DEFINITION OF TERMS

The history of inelastic electron scattering by multiphonon emission has recently been nicely reviewed in the introduction of a paper by Barmparis *et al.* [53]. Shi *et al.* have recently compared different numerical formalisms in this area [54,55]. The field has been seeing increased activity recently, including this work, as electronic structure methods are becoming reliable enough to treat the delicate physics of the electron-phonon interaction. We rely on density functional theory (DFT) in two different implementations: the embedded cluster approach, with orbitals expanded in local atom-centered basis functions, and periodic models based on supercells, with orbitals expanded in plane-wave basis sets.

The theoretical framework and numerical approximations used in this paper largely follow Alkauskas and co-workers [52], to which we refer the reader for a discussion of the validity of the major approximations and the motivations for choosing them. We will sketch their derivation here and note the differences in our approach, which has been tailored to the softer ionic nature of NaI compared to the semiconductor systems studied in Ref. [52]. Our system of interest is a NaI crystal with a single Tl atom occupying one of the sites on the Na sublattice, and we consider the situation of an extra electron introduced into this system. We start from Fermi's Second Golden Rule for the lifetime $\tau_{i\mathrm{I}}$ of the quantum state $|i\mathrm{I}\rangle$ [56,57],

$$\frac{1}{\tau_{i\mathrm{I}}} = \frac{2\pi}{\hbar} \sum_{fF \neq i\mathrm{I}} |\langle i\mathrm{I}|\widehat{H}^{\mathrm{ep}}|fF\rangle|^2 \delta(E_{i\mathrm{I}} - E_{fF}). \tag{1}$$

$\widehat{H}^{\mathrm{ep}}$ is the electron-phonon interaction Hamiltonian, which Eq. (1) treats to first order [52], $E_{i\mathrm{I}}$ is the energy of the state $|i\mathrm{I}\rangle$, and $\hbar = h/(2\pi)$ is Planck's reduced constant. There are three aspects of this expression that need to be approximated leading to three distinct types of approximations: the wave functions of the quantum states of the system must be expressed in a way that matrix elements of $\widehat{H}^{\mathrm{ep}}$ between them can be evaluated, the energies of the states must be found so that the δ-function can be evaluated, and $\widehat{H}^{\mathrm{ep}}$ itself must be approximated.

The full quantum state of the system is written as a product state. Lower-case Roman letters refer to electronic states, which depend explicitly on the electron coordinates and implicitly on the nuclear coordinates, while upper-case letters refer to vibrational states, which depend explicitly on the nuclear coordinates and implicitly on the electronic state: $|i\mathrm{I}\rangle = |i\rangle|\mathrm{I}\rangle$. This is the Born-Oppenheimer approximation; if the electronic states used are eigenstates for fixed atomic coordinates, as in this work, one has the static approximation [58]. We further approximate the electronic states as Slater determinants of Kohn-Sham (KS) orbitals; then $\widehat{H}^{\mathrm{ep}}$ connects states that differ by at most one orbital. Note that at least one of the electronic states is not the ground state, so there is an implicit independent-particle approximation (i.e., excited-state effects are neglected by using ground-state Kohn-Sham orbitals and eigenvalues) at this stage. The energies $E_{i\mathrm{I}}$ of the states are similarly taken to be the sum of electronic and vibrational energies. The former is estimated using DFT calculations that provide the orbitals, the details of which are given below. The latter are computed in a one-dimensional approximation in which a single effective phonon coordinate Q mediates the transition of interest [52] (in our case, the capture or release of an electron from a Tl dopant). This is a major approximation that reduces the high-dimensional phonon problem to a soluble 1D problem and permits a key advance of the current work: the avoidance of the harmonic approximation. The use of an effective 1D phonon space has been tested by Alkauskas *et al.* [59]. The nuclear dynamics are then determined (separately for each electronic state) by the 1D Schrödinger equation for a particle moving on an adiabatic potential energy surface (PES) computed within DFT in a given electronic configuration. Hence the (1D) vibrational wave functions depend on the electronic state. Within this framework, linearizing the electron-phonon interaction Hamiltonian (not the effective PES) in Q around $Q = Q_0$ gives the total electron-phonon matrix element in the form

$$\begin{aligned}\langle i\mathrm{I}||\widehat{H}^{\mathrm{ep}}|fF\rangle &= \langle i|\frac{\partial \widehat{H}^{\mathrm{ep}}}{\partial Q}|f\rangle\langle \mathrm{I}|Q - Q_0|F\rangle \\ &= W_{if}\langle \mathrm{I}|Q - Q_0|F\rangle.\end{aligned} \tag{2}$$

The electronic part is further approximated as

$$W_{if} = (\epsilon_f - \epsilon_i)\langle i|\frac{\partial f}{\partial Q}\rangle = (\epsilon_f - \epsilon_i)\frac{\partial}{\partial Q}\langle i(Q = Q_0)|\, f(Q)\rangle. \tag{3}$$

As indicated, the derivative is evaluated at $Q = Q_0$, consistent with the static approximation. The effective vibrational coordinate is related to locations of the atoms by [52]

$$Q^2 = \sum_l m_l(\vec{R}_l - \vec{R}_{0l})^2, \tag{4}$$

where m_l and $\vec{R}_l$ are, respectively, the mass and position of the atom at site l, and $\vec{R}_{0l}$ is the position of the atom at site l in a reference state corresponding to $Q = Q_0$. The $\vec{R}_{0l}$ and $\vec{R}_l$ are found by minimizing the energy of appropriate supercells or cluster models as described below. The sum runs over the entire crystal, but due to the localized nature of the trapped state, $\vec{R}_l - \vec{R}_{0l}$ tends to $\vec{0}$ as the distance between the lattice site l and the site of the Tl atom grows. In practice, we restrict all sums over l either to the cluster model being used for the electronic structure (when using local basis sets) or the first supercell (when using periodic boundary conditions). Q_0 corresponds to the state at which the expression is evaluated. The choice of Q_0 is discussed in Refs. [52,53]; in this work, we choose to evaluate Eq. (3) in the trapped state: $Q_0 = Q_{\max}$. Note that Eq. (2) is symmetric with respect to exchange of the initial and final states, but the symmetry is broken by the approximation of Eq. (3), which arbitrarily places the derivative on $|f\rangle$ and not $|i\rangle$. We checked the results presented below by computing $(\epsilon_f - \epsilon_i)\langle i|\frac{\partial f}{\partial Q}\rangle$ and $(\epsilon_i - \epsilon_f)\langle f|\frac{\partial i}{\partial Q}\rangle$ for the relevant orbitals (the choice of which is discussed below), finding agreement to better than 0.2%.

To relate estimates of trapping and detrapping time based on Eq. (1) to macroscopic phenomena, we assume the electronic system is in a definite charge state (Tl^+ for trapping, Tl° for detrapping) and a thermal population of the vibrational levels of the PES of the charge state. Hence, the final expression for the transition rate R is

$$R = g_i\frac{2\pi}{\hbar}\sum\nolimits_{\rm I} w_{\rm I}^i \sum\nolimits_F |\langle i{\rm I}|\widehat{H}^{\rm ep}|fF\rangle|^2\delta(E_{i{\rm I}} - E_{fF}), \tag{5}$$

where $w_{\rm I}^i$ is the Boltzmann occupation factor for the Ith vibrational level of the electronic state i, and g_i is the degeneracy of state i. Since there are eight equivalent [111] directions for the Tl to move when it traps an electron, and our double-well treatment of this state accounts for two of these, we set $g = 4$ for the trapped state. The ground state is nondegenerate, so $g = 1$ for the free electron. We further assume bimolecular kinetics for electron trapping (free electrons explore the crystal encountering distributed defects) and unimolecular kinetics for detrapping (each Tl^0 has the same probability to release its electron per unit time). In particular, for a physical sample of volume V containing a concentration of n_{Tl^+} Tl^+ atoms and n_{e^-} free electrons in the conduction band resulting in R_c electron trapping events per unit time per unit volume, we define the capture coefficient C_c by

$$R_c = C_c n_{e^-} n_{Tl^+} \tag{6}$$

and, similarly, the release rate per Tl^0 C_r by

$$R_r = C_r n_{Tl^0}, \tag{7}$$

where n_{Tl^0} is the concentration of Tl atoms that host trapped electrons. Hence below we calculate the rates in specific model systems containing a single Tl site in a given volume and a single extra electron. From the resulting rates we derive C_c and C_r. Alkauskas [52] further includes corrections that account for the modification of the extended (free) states by a charged defect. In the present case, we neglect these corrections since the Tl^+ dopant is an isovalent substituent for the Na^+, and the long-range Coulombic interaction between free e^- and Tl^+ is similar to that between free e^- and Na^+. Hence, we expect "free" electron states calculated in Tl-containing models to be fair representations of electron dynamics in the actual material.

III. METHODS AND APPROXIMATIONS

To calculate the potential energy surface (configuration-coordinate diagram, or cc-diagram) for the effective 1D phonon coordinate Q, the electronic transition energy, and the electron-phonon matrix elements, we use DFT. Two different formulations are used. The electronic transition energy and cc-diagram are computed with the VASP code [60–63] using a 64-atom model ($2 \times 2 \times 2$ supercell of the conventional eight-atom halite structure cell with one Na replaced by Tl). All but the valence electrons (1 per Na, 3 per Tl, and 7 per I atom) are pseudized using the projector-augmented-wave (PAW) [64,65] method (and standard VASP-provided PAW datasets) allowing us to expand the orbitals in basis sets determined by a 500 eV energy cutoff for each of the 8 k-points composing a regular $2 \times 2 \times 2$ grid in the Brillouin zone. During structural relaxations, all atomic coordinates and cell parameters were varied until the forces were less than 10^{-3} eV/Å. Electronic minimizations were converged to 10^{-6} eV. We refer to these calculations as plane-wave models (PWMs). We did not include corrections for the spin-orbit coupling in the valence- and conduction-band states, which we expect to be weak based on the slowness of the triplet-to-singlet radiative decay of (Tl+)* in NaI:Tl (the radiative lifetime is around 200 ns [33,66,67]). The electron-phonon matrix elements were computed using the NWCHEM package [68]. These calculations were run for a cluster model (CM), with no periodic boundary conditions, of 136 atoms ($Na_{67}TlI_{68}$) arranged in a roughly spherical shape with radius ~8 Å, centered on the Tl impurity. The initial positions were taken from previous work we have done on NaI [69]. As in that work, we have followed Govind *et al.* [70] to mimic the Ewald potential due to the remainder of the crystal not explicitly represented in our CM with an array of point charges occupying lattice sites outside the cluster boundary. During structural relaxations, 42 Na and 42 I atoms (the atoms further than 6 Å from the cluster center) on the exterior of the cluster were held fixed (enforcing the experimental lattice parameter). The remaining 52 atoms were fully relaxed. The convergence criteria were set (in atomic units) to 10^{-5}, 10^{-5}, and $10^{-3}/2$ for the energy, density, and gradients, respectively. CRENBL ECP basis sets [71–73] for Na and I sites, and Stuttgart RLC basis sets [73] for Tl, were used. Effective core potentials were used to pseudize all but

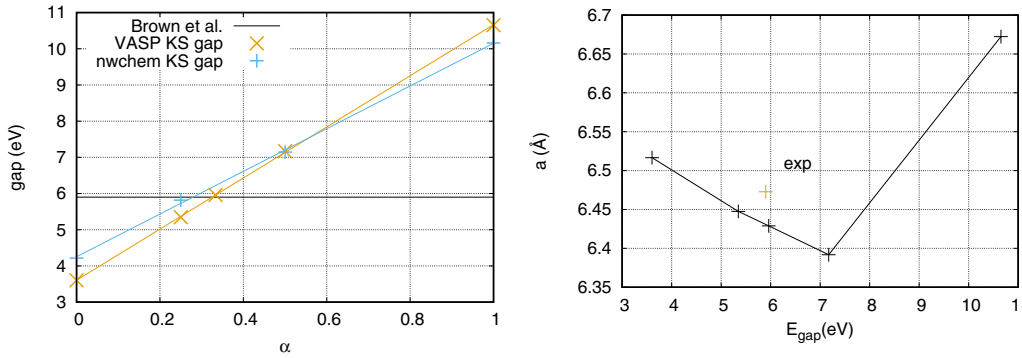

FIG. 1. Left: Band gap vs the fraction of explicit exchange included in the xc functional in our CM (blue) and PWM (yellow) calculations. Right: computed lattice constant a vs band gap for the PWM calculations. The experimental band gap is taken from Ref. [79] while the lattice constant is from Refs. [79,80]. The functionals are otherwise standard PBE for the remainder of the exchange functional and the correlation functional, except for the case $\alpha = 1$, which is Hartree-Fock (HF) theory (i.e., no correlation).

the valence electrons (9 per Na, 3 per Tl, and 7 per I atom). The CM calculations explicitly included the $2s$ and $2p$ Na electrons, while the PWM calculations did not.

IV. RESULTS AND DISCUSSION

A. Parametrization of the exchange-correlation approximation

Semilocal exchange-correlation (xc) approximations will not trap an electron on the Tl site [69], so at least some fraction of nonlocal exchange is needed to obtain even qualitatively correct behavior. As we will show below, the depth of the electron trap is sensitive to the xc approximation. Hence, the specific choice of xc approximation is a central decision for calculations such as those presented here. We have used the PBE0 [74–76] xc functional, but we adjusted the fraction α of explicit exchange [77,78] using the rationale that an xc approximation that "well"-represents the host material NaI is a good starting point for calculating the properties of isolated defects like the Tl_{Na} considered here. Using PWMs of pure NaI (using the primitive cell and converged $8 \times 8 \times 8$ k-point grids), we calculated the relaxed lattice parameters and KS gaps (at Γ) for $\alpha = {}^1/_n$, $n = 1, 2, 3, 4, \infty$. The results are summarized in Fig. 1, which also displays CM calculations of the KS gap at the fixed, experimental lattice parameter.

The left-hand panel of Fig. 1 shows that the predicted KS gap is linear in α with a positive correlation between the gap and α with semilocal PBE ($\alpha = 0$) exhibiting the DFT gap problem and $\alpha = 1$ exhibiting unphysically large exchange effects. The measured (at room temperature) onset of optical transitions to the conduction band [79] (composed primarily of Na s states) is marked with the black horizontal line. The CM calculations yield a lower slope in the gap versus α relation, which we attribute to the fixed geometry. We did not attempt to construct CMs at different lattice constants, but one could do so. The right-hand panel of Fig. 1 plots the KS gaps against the relaxed lattice constant for NaI. Room-temperature experimental data are also shown [80]. Based on these considerations, we chose $\alpha = {}^1/_3$ for the capture and release calculations presented below; we refer to the resulting xc approximation as $PBE0_{1/3}$. We will describe the combination of xc and cluster type, which we vary frequently in this work, with the notation "xc/cluster type" so that $PBE0_{1/3}$/PWM means a plane-wave model simulated using $PBE0_{1/3}$ (and all the other settings for VASP described above). The $PBE0_{1/3}$/PWM gives a lattice parameter of 6.429 Å (compared to the experimental value of 6.4728 Å [80]) and a KS gap of 5.989 eV (compared to the measured gap [79] of 5.9 eV).

B. Coordination environment of Tl^+ and Tl^0 in NaI and configuration coordinate diagram

Within $PBE0_{1/3}$, we relaxed both CMs and PWMs containing a Tl dopant. As we have found previously [69], the Tl occupies the Na lattice site with a small expansion of its host octahedron (the distance between Tl and near-neighbor I is 3.39 Å compared to ${}^a/_2 = 3.21$ Å NaI in the host material). Below we refer to this structure as the Tl-ground-state structure. To simulate the Tl^0 state, we introduced an extra electron. In the PWMs, which employ periodic boundary conditions that preclude a charged cell, the extra charge is compensated by a uniform background charge. We made no further corrections for the electrostatic interactions between the periodic images. We justify this approximation by noting that all energy differences were taken between cells with the same charge and similar dipole moments, so the leading corrections to the electrostatics cancel in the differences. Further, the electrostatic interaction between image charges is screened. With the extra electron, the lowest energy state in $PBE0_{1/3}$/PWM is obtained by displacing the Tl dopant along one of the eight equivalent [111] directions by 0.702 Å [putting the Tl^0 structure at $Q_{\max} = 13.53\,\text{amu}^{1/2}$ Å with this Tl^+ state at $Q = 0$ according to Eq. (4)]. The Tl^0 state is 0.242 eV more stable than an extra electron in the Tl-ground-state structure. In $PBE0_{1/3}$/CM, there is a local minimum corresponding to the Tl^0 state, but it is 0.123 eV higher in energy than the Tl-ground-state structure (of the $PBE0_{1/3}$/CM). The reason for this is that the Tl is displaced only 0.545 Å ($Q_{\max} = 11.85\,\text{amu}^{1/2}$ Å) in $PBE0_{1/3}$/CM; we conclude that the CM is not large enough to accommodate the strain field associated with the displaced Tl resulting in destabilization due to compression against the hard wall of the fixed outer shell of the CM. This conclusion is somewhat counterintuitive since the CM actually has more atoms than the PWM

TABLE I. Distance along the effective phonon coordinate Eq. (4) between the Tl-ground-state structure and the Tl^0 structure for several xc functionals in CM and PWM calculations.

xc functional	α	Q_{max}PWM(amu$^{1/2}$ Å)	Q_{max}CM(amu$^{1/2}$ Å)
PBE0(=$PBE0_{1/4}$)	0.25		11.47
HSE06	0.25	11.18	
$PBE0_{1/3}$	1/3	13.53	11.85
BHH	0.5		12.07
HF	1		12.77

(136 compared to 64). However, fewer of the atoms can move in the CM (52 compared to 64). Additionally, the periodic boundary conditions of the PWM are more flexible than the fixed boundary conditions of the CM. For example, in the PWM, the displacements along the (111) column that contains the Tl are all nonzero (with the second-neighbor Na atoms moving perpendicular to the column). In contrast, in the CM all (both) the Na in the (111) column containing Tl are fixed, constraining the near-neighbor I atoms more in the CM than in the PWM.

Our previous work on this system [69] used the same CMs employed here to model self-trapped exciton migration in pure NaI. That work used the Becke half-and-half [81,82] (BHH) xc functional ($\alpha = 1/2$) and found good agreement for predicted absorption and emission energies for the self-trapped exciton. We also computed the electron trapping using BHH/CMs. We found $Q_{max} = 12.07$ using BHH/CMs. Some other exchange-correlation functionals were also explored; results are listed in Table I. We speculate that the off-center displacement of the Tl and the resulting compressive forces upon electron trapping are more difficult to accommodate in CMs than the tensile forces that result when an exciton self-traps. Simulating the self-trapped exciton using PWMs is beyond the scope of the current work, but it is certainly a worthy objective to investigate convergence with respect to model size, which remains an important issue for calculations requiring hybrid xc functionals. The local coordination environment of the Tl in the ground-state and trapped electron structures is depicted in Fig. 2.

We then linearly interpolated between the ground-state and trapped electron structures to produce a sequence of structures between $Q = 0$ and $Q = Q_{max}$, and we performed single-point energy calculations starting from orbitals derived from either the Tl^0 state or the Tl-ground-state structure. In both cases, the extra electron was included. The results of this procedure produce the cc-diagram, plotted in Fig. 3 for a variety of approximations. These results show that the trap depth is sensitive to both the exchange-correlation approximation and the type of model (CM or PWM) used. Achieving the same trap depth in a CM as a PWM requires larger α. While we calculated rough configuration-coordinate diagrams for a variety of DFT approximations, we only carried out the trapping rate calculations for $PBE0_{1/3}$ using the PWM.

C. Vibrational levels and wave functions

With the relevant vibrational dynamics around the Tl center described by an effective 1D Schrödinger equation, the task of finding the vibrational structure is equivalent to finding the rotationless states of a single diatomic molecule (with Q taking the place of the bond length, and the effective 1D PES taking the place of the interatomic potential in the radial Schrödinger equation). To compute the vibrational levels and wave functions for the motion of the effective phonon coordinate Q, we used the LEVEL [83] program by LeRoy, which is based on software originally written by Zare [84] for finding the rovibrational levels of diatomic molecules. The eigenvalues are searched for by integrating solutions from the classically forbidden regions at high and low Q toward each other and adjusting the eigenvalue to eliminate the discontinuity in the slope where the two solutions meet. When an eigenvalue is found that supports a smooth solution to the 1D Schrödinger equation satisfying the boundary conditions on both sides of the classically allowed region, the solution is tabulated, and the code starts searching for a higher eigenvalue or stops if enough solutions have been found.

This approach requires the values of the PES's well into the classically forbidden region, so the computed *ab initio* points were extended to high and low Q as follows. First, the crystal symmetry implies that the 1D PES's for the trapped

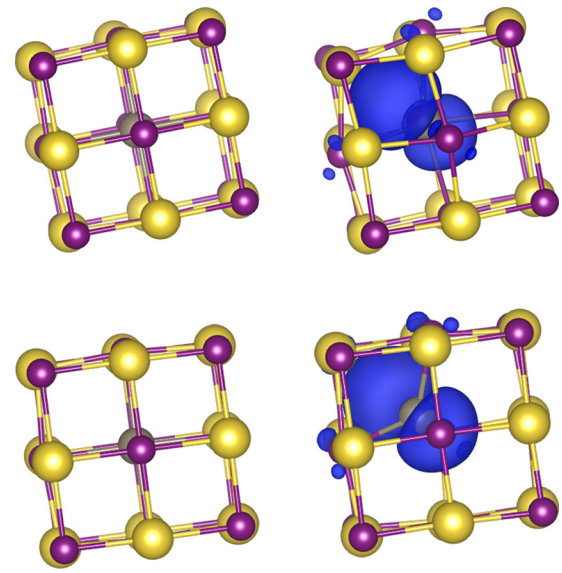

FIG. 2. Calculated local environment of a Tl dopant in NaI using the $PBE0_{1/3}$ exchange-correlation approximation in plane-wave (top row) and cluster (bottom row) models without (left column) and with (right column) a trapped electron. The spin-density isosurfaces (at 0.001 electrons per cubic angstrom) associated with the trapped electron are plotted in blue. Na atoms are shown in gold, I atoms in purple, and the Tl dopant is gray.

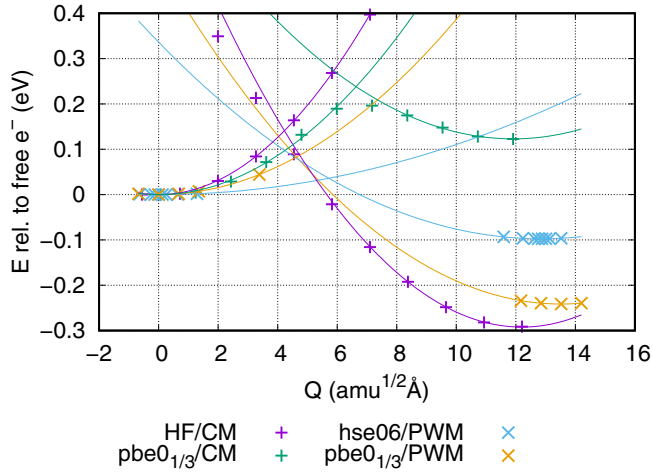

FIG. 3. Configuration coordinate diagram calculated using either cluster models (+'s) or periodic boundary conditions (×'s) and HF (purple), HSE06 (blue), or $PBE0_{1/3}$ (yellow and green). The origin of the energy scale is the energy of a free electron in the ground-state Tl^+ structure, and the abscissa is Q, the effective 1D phonon coordinate. Solid lines are quadratic fits near the appropriate minimum. See the text for details.

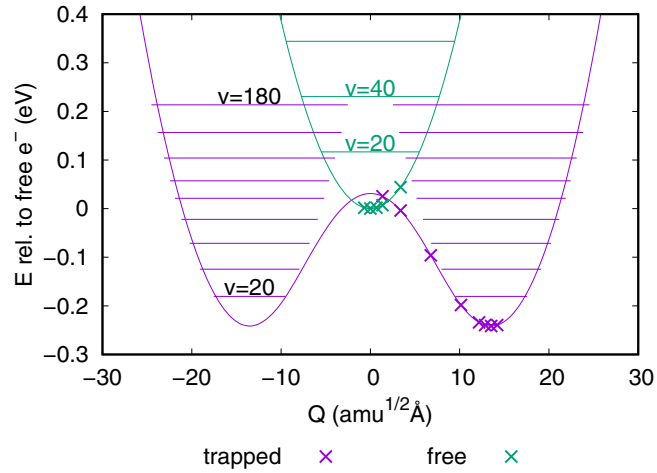

FIG. 4. Final configuration-coordinate diagram used for calculation of the vibrational structure. The ×'s mark explicitly calculated points (and agree with the green ×'s in Fig. 3), the curved solid lines are the interpolated/extrapolated adiabatic potential energy surfaces, and the horizontal solid lines mark every 20th vibrational level (excluding the $v = 0$ levels for clarity), drawn between the classical turning points in the harmonic approximation.

and free states are symmetric about $Q = 0$ (with motion in the positive and negative directions moving to Tl^0 states with Tl displacements along two equivalent [111] directions). Hence reflections through $Q = 0$ of the directly computed points on each PES were added. The free state was well fit by a parabola that was used as the final PES at all Q. For the trapped state, a finely sampled PES in the range of the directly calculated points was generated by interpolation via a cubic spline. The Tl^0 PES was extended beyond the computed data by a parabolic fit determined by the last three points. This procedure results in a double-well trapped PES that is symmetric about $Q = 0$ and has continuous derivatives up to the second one. The final PES's are displayed in Fig. 4.

The vibrational levels (labeled by the single quantum number $v \geqslant 0$) belonging to the trapped and free PES's were then found numerically. The reflection symmetry implies that the levels can be classified by parity with the wave function for each state having zero in either the function value (v odd) or the first derivative (v even) at $Q = 0$. We searched for solutions starting with the correct behavior at $Q = 0$ with various trial eigenvalues until all the symmetric and antisymmetric levels were found. A horizontal line between the classical turning points in the harmonic approximation is drawn at the vertical coordinate corresponding to the eigenvalue of every 20th level beyond $v = 2$ for both the trapped and free surfaces, as shown in Fig. 4. The final calculations presented here considered 297 vibrational levels of the trapped PES spanning 0.84 eV. The free electron state was described with 201 vibrational levels spanning 1.15 eV. The harmonic level spacing in the free state is 45.8 cm^{-1} (5.68 meV) and falls in the upper part of the acoustic modes of the NaI host material, consistent with the large mass of Tl compared to the Na that it substitutes. The deep levels of the trapped PES are doubly degenerate and have spacings around 23.48 cm^{-1} (2.91 meV), while the levels above the barrier have close to the same spacing corresponding to the combination of the two separate wells to form one large well with twice the width.

With the vibrational wave functions determined for both states, the matrix elements $\langle \mathrm{I}|Q|F\rangle$ appearing in Eq. (2) were determined using numerical quadrature. Since the upper PES is a parabola, the corresponding vibrational wave functions are the well-known harmonic-oscillator functions, which are expressible analytically. However, we treated them numerically using the same procedures for both the upper and lower PES's. As a check on the LEVEL solver, we compared the first few wave functions to the expected harmonic-oscillator functions and found excellent agreement. Since Q is an odd operator, $\langle \mathrm{I}|Q|F\rangle$ vanishes unless $|\mathrm{I}\rangle$ and $|F\rangle$ are of opposite parity. We chose to evaluate all the matrix elements, using this parity selection rule as a post hoc numerical check. In our calculations, the ratio of nearby allowed and forbidden matrix elements is around 10^9 (or 18 orders of magnitude in the transition rate, which is proportional to the square of the matrix element).

D. Electron-phonon coupling

The final ingredient needed to evaluate the transition rates is the electron-phonon coupling of Eq. (3). As stated above, these calculations were done using CMs. Two quantities are needed to evaluate Eq. (3): the eigenvalues of the initial and final electron orbitals in the trapped state and the derivative $\langle i|\frac{\partial f}{\partial Q}\rangle$. We modified the NWChem implementation of the frontier molecular orbital electron transfer approach of Farazdel *et al.* [85] to compute the derivative $\langle i|\frac{\partial f}{\partial Q}\rangle$. In calculations using local basis sets, the bases are generally nonorthogonal so that the overlap between two orbitals $\langle i|f\rangle$ is computed using $\langle i|f\rangle = c_i^\dagger S c_f$, where c_i and c_f are column vectors of coefficients describing the orbitals in the basis, and S is the overlap matrix, which coincides with the

identity matrix for orthonormal bases. To estimate the derivative $\langle i|\frac{\partial f}{\partial Q}\rangle$ using finite differences, we constructed a combined geometry in which every atom appears twice: once at the position corresponding to $Q = Q_{\max}$ and once at the (possibly identical) position corresponding to $Q = Q_{\max} + \delta Q$. The basis sets were similarly combined. The overlap matrix of the combined geometry (which is now of twice the rank of the original overlap matrices) was then generated. Overlaps between orbitals expressed in either geometry could then be found by using the appropriate block of the combined overlap matrix. We used $\delta Q = -Q_{\max}/100$. The initial and final electronic orbitals $|i\rangle$ and $|f\rangle$ must be determined. The orbital occupied by the trapped electron is obvious since the motion of the Tl from its equilibrium Tl^+ position to the Tl^0 minimum pulls a single occupied Tl p-orbital well into the gap. The symmetry-breaking of the Tl displacement stabilizes the trapping orbital with lobes along the soft [111] direction of NaI, leading to a sensitive dependence of the trapping orbital shape on Q and a correspondingly large $\langle i|\frac{\partial f}{\partial Q}\rangle$ reflecting the strong interaction between electrons in this orbital and the lattice vibrations. This strong interaction explains why Tl is an effective electron trap in NaI:Tl. This strong trapping behavior allows Tl to outcompete other (optically inactive) traps present in NaI, which leads to the high light yield of NaI:Tl. The choice of the free electron orbital is more arbitrary. We choose the conduction-band minimum orbital to describe the free electron. This orbital is comprised primarily by the s-orbitals of the Na atoms in the second coordination shell of the Tl. For the case of trapping thermalized free electrons, the appropriate initial state to consider is a thermal ensemble of the empty states $|i\mathrm{I}\rangle$. The CBM orbital is the only one with appreciable electron-phonon coupling W_{if} within several k_BT of the CBM at room temperature. In the case of detrapping, the initial state is a thermal population of the levels of trapped double-well potential shown in Fig. 4. For transitions to occur, therefore, there must be thermal population of a vibrational state of the trapped PES with energy at least as large as the ground vibrational state of the final electronic state. Figure 5 shows the density of states (DOS) from the region near the CBM (in both computational settings) along with sticks to indicate the strength of the electron-phonon coupling of each state. Most of the unoccupied electronic states have small couplings because the orbitals do not involve the Tl or neighboring atoms and hence have little overlap with the trapping Tl p-orbital. In both cases (trapping and detrapping), then, we expect the CBM orbital to be the dominant upper electronic level. Hence, the capture and release coefficients presented below consider only transitions between the trapping Tl p-orbital and the CBM orbital. Our calculation gives $W_{if} = 1.08 \times 10^{-3}\,\mathrm{eV\,AMU^{1/2}\,Å}$ for the electronic matrix element between the trapping orbital and the CBM.

E. Electron capture and release rates

The combination $\sum_{\mathrm{I}} w_{\mathrm{I}}^i \sum_F |\langle \mathrm{I}|Q|F\rangle|^2 \delta(E_{i\mathrm{I}} - E_{fF})$ was constructed as a function of T (which enters only through the thermal occupation factors w_{I}^i, which in turn were computed by direct summation of the vibrational partition function at each T over the available vibrational states) for trapping and detrapping cases. The δ-function was approximated by a Gaussian of full width at half-maximum (FWHM) 2.5 meV; the final release rates were tested to make sure they did not depend sensitively on the width. The final release rate and electron capture coefficient were then simply obtained from Eq. (5). These quantities are the primary result of this work and are plotted in Fig. 6, where they are compared to available data from the analysis of thermally stimulated luminescence (TSL) experiments [5,51] and of a kinetic Monte Carlo model of scintillation [33] fitted to scintillation decay curves. To explore the sensitivity of these calculations to errors in the electronic structure, we have plotted results obtained by shifting the trap depth up and down by 0.1 eV (an arbitrary value

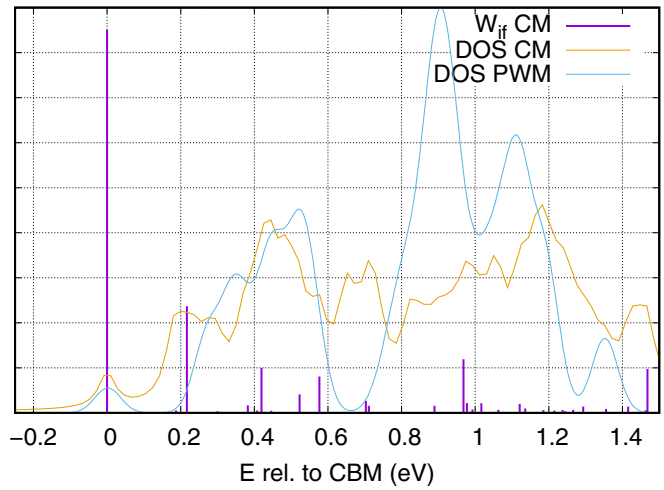

FIG. 5. Electron-phonon matrix elements and density of states from CM calculations and density of states from PWM calculations near the conduction-band minimum.

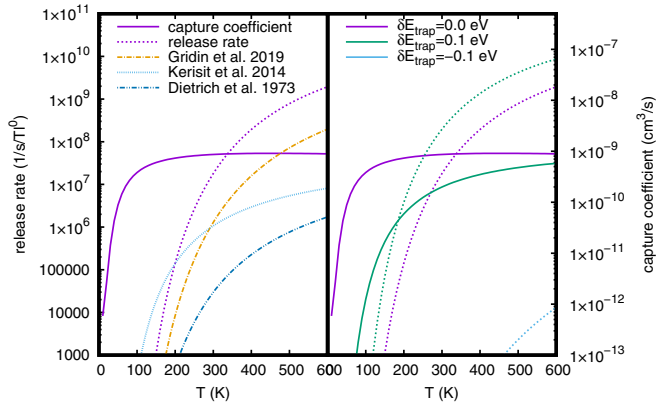

FIG. 6. Capture coefficient (solid lines) and release rate (broken lines) as a function of temperature. The calculated values, shown in both panels, are in black. In the left panel, the theoretical release rate (dotted purple) is compared to Arrhenius curves from thermally stimulated luminescence measurements by Dietrich *et al.* [5] and Gridin *et al.* [51] as well as an Arrhenius curve resulting from analysis of scintillation decay curves by Kerisit *et al.* [33]. In the right panel, our predictions (purple) are compared to values that we would obtain if the trapped state was shifted by $\delta E = 0.1\,\mathrm{eV}$ (green) or $\delta E = -0.1\,\mathrm{eV}$ (blue) in energy. The capture rate for $\delta E = -0.1\,\mathrm{eV}$ is below the bottom of the graph.

that we believe is larger than the actual error). This exercise shows that the results are especially sensitive to shifts toward a deeper trap ($\delta E < 0$), which lower both capture and release rates by more than four orders of magnitude over the entire temperature range considered.

1. Release

The calculated release rate exhibits approximately Arrhenius behavior. A fit of the curve to Ae^{-E/k_BT} yields $A = (2.37 \pm 0.01) \times 10^{11}$ s^{-1} and $E = 0.2450 \pm 0.0001$ eV. The latter is close to, but does not agree with, either the trap depth (0.242 eV) or the energy difference between the ground vibrational states of the trapped and free PES's (0.241 eV). This is a textbook thermally activated process: as the temperature is raised, detrapping commences when there is thermal population in trapped states of high enough energy to transition into the ground vibrational state of the Tl^+ configuration. We also note that the shape of the lower (Tl^0) PES, which results from the soft nature of the crystal, has a large effect on the magnitude of the release rates, which is determined by the tail of the vibrational wave functions that extends to near $Q = 0$, where the low-lying Tl^+ state wave functions are nonvanishing. Hence, calculations done in the harmonic approximation, including Refs. [52,53] and all other theoretical works of which we are aware, will badly underestimate the rates in situations such as this one.

The comparison of the release rate to the thermally stimulated luminescence experiments deserves comment. These experiments are performed by subjecting the cold ($T \sim 10$ K) sample to x rays to develop an initial population of trapped excitations followed by gradual heating. As the sample warms, thermal detrapping occurs leading to luminescence, which is measured. There is a large discrepancy in the release rates reported in Refs. [5] and [51], with Gridin's larger release rates (green dash-dot trace in Fig. 6) much closer to the theoretical calculations of this work (yellow dots). As discussed in detail by Gridin, the difference between these curves stems not from differences in the measured luminescence, but in the method of analysis. In fact, Gridin presents two analyses in Ref. [51]. The first uses the same analysis method as Ref. [5], which consists of fitting the initial rise of the glow peak resulting from electron release from Tl^0 to the Arrhenius form. The second analysis of Gridin *et al.* is based on a more sophisticated model that uses data from the entire glow peak. Based on simulations of the TSL curves for NaI doped with three different activators, Gridin *et al.* deem their estimates to be some of the most reliable experimental determinations available for thermal release of electrons from Tl^0 in NaI. Our theoretical simulations agree well with Refs. [5,51] with regard to the shape of the release versus T curve (i.e., Arrhenius behavior with a trap depth near 0.26 eV). The magnitudes of the theoretical release rates presented here are greater than the best available experimental estimates by a factor of "only" around 14. Given that slight differences in the TSL analysis change the magnitude of the release rate by a factor of approximately 44, we consider the agreement with the whole-peak fitting procedure of Ref. [51] to be fairly good. It appears that the experimental and theoretical pictures are converging.

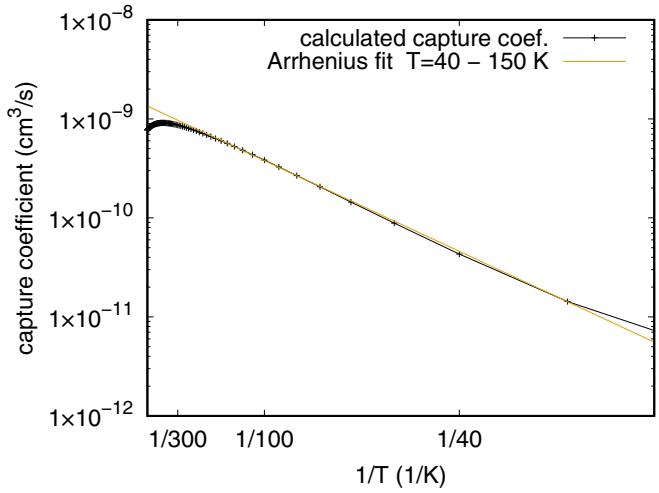

FIG. 7. Arrhenius fit (yellow line) to the calculated capture coefficient (decorated black curve—same data as the solid purple curve in Fig. 6).

2. Capture

In contrast to the release processes, which are very well described by the Arrhenius equation, the capture coefficient arising from our theoretical treatment is not. In fact, the capture coefficient curve (solid purple line in Fig. 6) exhibits a maximum around $T = 450$ K, decreasing at higher temperatures. Even at practically relevant temperatures for γ-ray detection (i.e., room temperature), our predicted capture coefficient is around 10% lower than suggested by an Arrhenius fit (presented in Fig. 7). We carefully checked that this effect is not a reflection of unconverged calculations. For example, removing the highest 100 vibrational levels of the Tl^0 state (the final states for the capture transition) results in a decrease of the calculated capture rate at $T = 1000$ K of less than 1%.

The origin of the suppression of capture at high temperatures turns out to be a kind of anharmonic effect arising from resonance of the vibrational states from the double-well Tl^0 PES with the thermally occupied levels of the Tl^+ upper state. Figure 8 shows color intensity plots of the transition strengths $|\langle \mathrm{I}|Q|F\rangle|^2$. The top panel shows all the states considered; the bottom panel is zoomed into the region of phase space in which the transitions occur.

The double-well structure of the lower PES leads to interesting patterns in Fig. 8. States of the lower (Tl^0) PES with $v < 92$ have eigenvalues below the barrier between the two wells, and there is a region around $Q = 0$ that is classically forbidden for these states. Higher-lying states have no classically forbidden region between the two wells and are separated in Fig. 8 from the lower-lying states by a dark band. The fine checkerboard pattern evident in the bottom panel results from the parity selection rule discussed above. The energy-conserving δ-function of Eq. (5) is satisfied for pairs of upper and lower states marked with green +'s in Fig. 8. Efficient trapping occurs between pairs of states that have large transition strengths (indicated by the color scale) and fall on the line of green +'s. So far, our discussion of Fig. 8 applies equally to trapping and detrapping. The temperature dependence of the capture rates in our supercell (and hence the

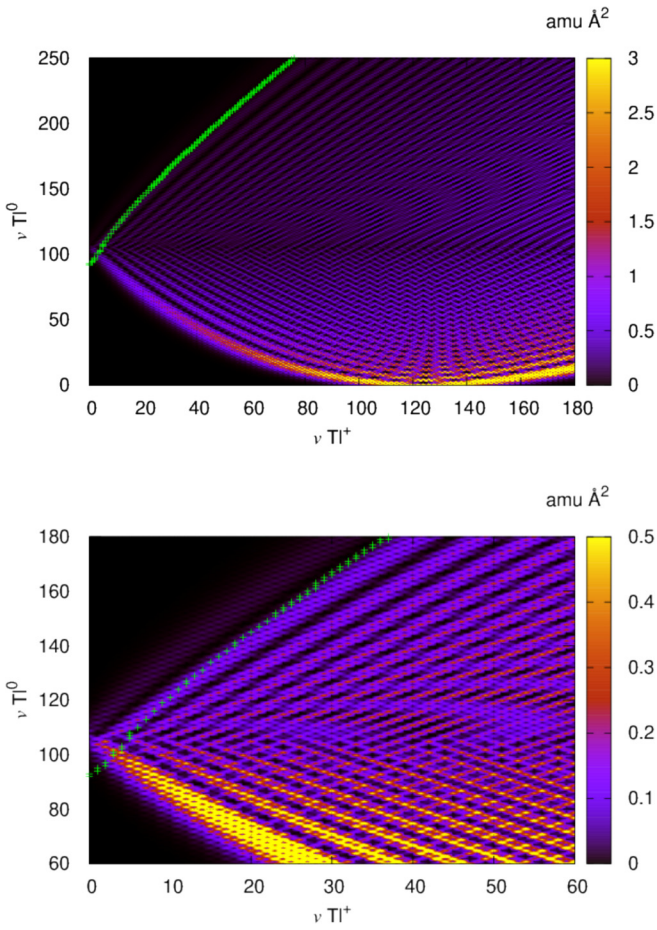

FIG. 8. Heat map of the squared matrix elements $|\langle \mathrm{I}|Q|F\rangle|^2$ between different vibrational states of the upper (horizontal axis) and lower (vertical axis) PES's. The green +'s mark transitions that are allowed by energy conservation. Since none of the plotted quantities involves the thermal occupation factors, this figure describes both trapping and detrapping probabilities.

final capture coefficient) arises from the thermal populations of the upper states, which correspond to the horizontal axis in Fig. 8. The strongest transitions that conserve energy have low vibrational quantum numbers in the upper state. As the temperature is increased, the thermal occupation of these states is lowered as they lose occupancy to higher-lying states that are inaccessible at low T.

Figure 8 clearly shows that fine details of the PES's (e.g., the height of the barrier of the lower PES relative to the minimum of upper state) determine the temperature dependence of the transition rates through a complicated interplay between the matrix elements and the locus of energy-conserving transitions. Figure 3 clearly shows that such details of the cc-diagram are quite sensitive to the xc approximation used, underlying the need to have a good description of the energetics of both initial and final states for the type of simulations presented here. The right-hand panel of Fig. 6 can be interpreted in terms of Fig. 8. Errors in the trap depth shift the locus of energy-conserving transitions up for shallower traps and down for deeper traps. In particular, the decrease in capture rate as the trapped state is raised toward the CBM can be understood by noting that shifting the green +'s up in Fig. 8 moves them to the less intense parts of the color map.

V. CONCLUSIONS

We have used state-of-the-art hybrid density functional theory electronic structure methods, capable of reliably representing both extended and localized electronic states, to explore the adiabatic PES's involved in transitions of the charge state of Tl dopants in NaI:Tl. Due to the soft nature of NaI, we have found significant departures from harmonic behavior. Numerical methods from gas phase diatomic spectroscopy have been adapted to the current problem, yielding a method that can treat PES's of arbitrary shape. We have implemented a method to estimate the electron-phonon coupling using a local-orbital description of the electronic states involved in trapping and detrapping of electrons on Tl sites. From these ingredients, we have calculated trapping and detrapping rates in agreement with available data. Our numerical calculations elucidate the manner in which the symmetry of the trapping orbital interacts with the facile motion of the Tl to produce efficient trapping centers that make NaI:Tl a bright scintillator. We predict, surprisingly, that the capture rate for electrons should decrease as T is raised above 450 K. The success of this work shows that modern electronic structure methods have the capacity, if used carefully, to treat delicate problems of microscopic dynamics following excitation, yielding information that is difficult to access experimentally.

ACKNOWLEDGMENTS

This research was supported by the National Nuclear Security Administration, Office of Defense Nuclear Nonproliferation Research and Development of the US Department of Energy (DOE). The calculations were performed using PNNL Institutional Computing at the Pacific Northwest National Laboratory. PNNL is operated by Battelle for the US DOE under Contract No. DE-AC05-76RL01830. The authors acknowledge Sergii Gridin and Richard Williams for advance access to their TSL data and useful discussions.

[1] G. F. Knoll, *Radiation Detection and Measurement* (Wiley, New York, 2000).
[2] R. Hofstadter and M. H. Stein, IEEE Trans. Nucl. Sci. **22**, 13 (1975).
[3] R. W. Birkmire, R. B. Murray, and M. Luntz, Phys. Rev. B **15**, 31 (1977).
[4] H. B. Dietrich and R. B. Murray, J. Lumin. **5**, 155 (1972).
[5] H. B. Dietrich, A. E. Purdy, R. B. Murray, and R. T. Williams, Phys. Rev. B **8**, 5894 (1973).
[6] F. J. Keller and R. B. Murray, Phys. Rev. **150**, 670 (1966).
[7] R. B. Murray, IEEE Trans. Nucl. Sci. **22**, 54 (1975).
[8] R. B. Murray and F. J. Keller, Phys. Rev. **137**, A942 (1965).

[9] R. D. Popp and R. B. Murray, J. Phys. Chem. Solids **33**, 601 (1972).
[10] R. G. Fuller, R. T. Williams, and M. N. Kabler, Phys. Rev. Lett. **25**, 446 (1970).
[11] R. T. Williams and M. N. Kabler, Phys. Rev. B **9**, 1897 (1974).
[12] R. T. Williams and K. S. Song, J. Phys. Chem. Solids **51**, 679 (1990).
[13] R. T. Williams, K. S. Song, W. L. Faust, and C. H. Leung, Phys. Rev. B **33**, 7232 (1986).
[14] G. Bizarri, N. J. Cherepy, W. S. Choong, G. Hull, W. W. Moses, S. A. Payne, J. Singh, J. D. Valentine, A. N. Vasilev, and R. T. Williams, IEEE Trans. Nucl. Sci. **56**, 2313 (2009).
[15] G. Bizarri, W. W. Moses, J. Singh, A. N. Vasil'ev, and R. T. Williams, J. Lumin. **129**, 1790 (2009).
[16] G. Bizarri, W. W. Moses, J. Singh, A. N. Vasil'Ev, and R. T. Williams, J. Appl. Phys. **105**, 044507 (2009).
[17] G. Bizarri, W. W. Moses, J. Singh, A. N. Vasil'Ev, and R. T. Williams, Phys. Status Solidi C **6**, 97 (2009).
[18] J. Q. Grim, Q. Li, K. B. Ucer, A. Burger, G. A. Bizarri, W. W. Moses, and R. T. Williams, Phys. Status Solidi A **209**, 2421 (2012).
[19] J. Q. Grim, K. B. Ucer, A. Burger, P. Bhattacharya, E. Tupitsyn, E. Rowe, V. M. Buliga, L. Trefilova, A. Gektin, G. A. Bizarri, W. W. Moses, and R. T. Williams, Phys. Rev. B **87**, 125117 (2013).
[20] H. Huang, Q. Li, X. Lu, Y. Qian, Y. Wu, and R. T. Williams, Phys. Status Solidi RRL **10**, 762 (2016).
[21] M. Prange, D. Wu, Y. Xie, L. W. Campbell, F. Gao, and S. Kerisit, *Hard X-Ray, Gamma-Ray, and Neutron Detector Physics XVI*, edited by A. Burger, L. Franks, R. B. James, and M. Fiederle (SPIE, 2014), Vol. 9213, pp. 106–122.
[22] Q. Li, J. Q. Grim, K. B. Ucer, A. Burger, G. A. Bizarri, W. W. Moses, and R. T. Williams, Phys. Status Solidi RRL **6**, 346 (2012).
[23] Q. Li, J. Q. Grim, R. T. Williams, G. A. Bizarri, and W. W. Moses, Nucl. Instrum. Methods Phys. Res., Sect. A **652**, 288 (2011).
[24] Q. Li, J. Q. Grim, R. T. Williams, G. A. Bizarri, and W. W. Moses, J. Appl. Phys. **109**, 123716 (2011).
[25] Q. Li, R. T. Williams, and D. Berg, Phys. Status Solidi B **250**, 233 (2013).
[26] X. Lu, Q. Li, G. A. Bizarri, K. Yang, M. R. Mayhugh, P. R. Menge, and R. T. Williams, Phys. Rev. B **92**, 115207 (2015).
[27] W. W. Moses, G. A. Bizarri, R. T. Williams, S. A. Payne, A. N. Vasil'Ev, J. Singh, Q. Li, J. Q. Grim, and W. S. Choong, IEEE Trans. Nucl. Sci. **59**, 2038 (2012).
[28] V. Pankratov, A. I. Popov, L. Shirmane, A. Kotlov, G. A. Bizarri, A. Burger, P. Bhattacharya, E. Tupitsyn, E. Rowe, V. M. Buliga, and R. T. Williams, Radiat. Meas. **56**, 13 (2013).
[29] K. B. Ucer, G. Bizarri, A. Burger, A. Gektin, L. Trefilova, and R. T. Williams, Phys. Rev. B **89**, 165112 (2014).
[30] R. T. Williams, J. Q. Grim, Q. Li, K. B. Ucer, G. A. Bizarri, and A. Burger, in *Excitonic and Photonic Processes in Materials*, Springer Series in Materials Science, Vol. 203, edited by J. Singh and R. Williams (Springer, Singapore, 2015), pp. 299–358.
[31] R. T. Williams, J. Q. Grim, Q. Li, K. B. Ucer, and W. W. Moses, Phys. Status Solidi B **248**, 426 (2011).
[32] S. Kerisit, K. M. Rosso, B. D. Cannon, F. Gao, and Y. Xie, J. Appl. Phys. **105**, 114915 (2009).
[33] S. Kerisit, Z. G. Wang, R. T. Williams, J. Q. Grim, and F. Gao, IEEE Trans. Nucl. Sci. **61**, 860 (2014).
[34] S. Kerisit, K. M. Rosso, and B. D. Cannon, IEEE Trans. Nucl. Sci. **55**, 1251 (2008).
[35] M. P. Prange, L. W. Campbell, and S. Kerisit, Phys. Rev. B **96**, 104307 (2017).
[36] M. P. Prange, L. W. Campbell, D. Wu, F. Gao, and S. Kerisit, Phys. Rev. B **91**, 104305 (2015).
[37] A. N. Vasil'Ev and A. V. Gektin, IEEE Trans. Nucl. Sci. **61**, 235 (2014).
[38] M. P. Prange, Y. Xie, L. W. Campbell, F. Gao, and S. Kerisit, J. Appl. Phys. **122**, 234504 (2017).
[39] R. Devanathan, L. R. Corrales, F. Gao, and W. J. Weber, Nucl. Instrum. Methods A **565**, 637 (2006).
[40] S. A. Payne, N. J. Cherepy, G. Hull, J. D. Valentine, W. W. Moses, and W.-S. Choong, IEEE Trans. Nucl. Sci. **56**, 2506 (2009).
[41] A. N. Vasil'ev, IEEE Trans. Nucl. Sci. **55**, 1054 (2008).
[42] S. Lam, S. E. Swider, A. Datta, and S. Motakef, IEEE Trans. Nucl. Sci. **62**, 3397 (2015).
[43] K. Yang and P. R. Menge, J. Appl. Phys. **118**, 213106 (2015).
[44] N. V. Shiran, A. V. Gektin, Y. Boyarintseva, S. Vasyukov, A. Boyarintsev, V. Pedash, S. Tkachenko, O. Zelenskaya, N. Kosinov, O. Kisil, and L. Philippovich, IEEE Trans. Nucl. Sci. **57**, 1233 (2010).
[45] T. Shalapska, F. Moretti, E. Bourret, and G. Bizarri, J. Lumin. **202**, 497 (2018).
[46] I. V. Khodyuk, S. A. Messina, T. J. Hayden, E. D. Bourret, and G. A. Bizarri, J. Appl. Phys. **118**, 084901 (2015).
[47] A. V. Gektin, A. N. Belsky, and A. N. Vasil'ev, IEEE Trans. Nucl. Sci. **61**, 262 (2014).
[48] Q. G. Feng and K. Biswas, J. Appl. Phys. **120**, 213104 (2016).
[49] R. H. Bartram, L. A. Kappers, D. S. Hamilton, A. Lempicki, C. Brecher, V. Gaysinskiy, E. E. Ovechkina, and V. V. Nagarkar, IEEE Trans. Nucl. Sci. **55**, 1232 (2008).
[50] M. S. Alekhin, J. T. M. de Haas, I. V. Khodyuk, K. W. Krämer, P. R. Menge, V. Ouspenski, and P. Dorenbos, Appl. Phys. Lett. **102**, 161915 (2013).
[51] S. Gridin, R. T. Williams, A. Belsky, E. Galenin, A. Gektin, N. Shiran, S. Vasiukov, and A. Vasil'ev, J. Phys. Chem. C **123**, 13519 (2019).
[52] A. Alkauskas, Q. Yan, and C. G. Van de Walle, Phys. Rev. B **90**, 075202 (2014).
[53] G. D. Barmparis, Y. S. Puzyrev, X. G. Zhang, and S. T. Pantelides, Phys. Rev. B **92**, 214111 (2015).
[54] L. Shi, K. Xu, and L.-W. Wang, Phys. Rev. B **91**, 205315 (2015).
[55] L. Shi, K. Xu, and L.-W. Wang, Phys. Rev. B **97**, 077302 (2018).
[56] P. A. M. Dirac, Proc. R. Soc. A **114**, 243 (1927).
[57] G. D. Mahan, *Many-Particle Physics*, Physics of Solids and Liquids (Springer, New Delhi, 2000).
[58] M. G. Burt, J. Phys. C **16**, 4137 (1983).
[59] A. Alkauskas, J. L. Lyons, D. Steiauf, and C. G. Van de Walle, Phys. Rev. Lett. **109**, 267401 (2012).
[60] G. Kresse and J. Furthmuller, Phys. Rev. B **54**, 11169 (1996).
[61] G. Kresse and J. Furthmüller, Comput. Mater. Sci. **6**, 15 (1996).
[62] G. Kresse and J. Hafner, Phys. Rev. B **47**, 558 (1993).
[63] G. Kresse and J. Hafner, Phys. Rev. B **49**, 14251 (1994).
[64] P. E. Blochl, Phys. Rev. B **50**, 17953 (1994).

[65] G. Kresse and D. Joubert, Phys. Rev. B **59**, 1758 (1999).
[66] W. S. Choong, G. Bizarri, N. J. Cherepy, G. Hull, W. W. Moses, and S. A. Payne, Nucl. Instrum. Methods A **646**, 95 (2011).
[67] J. S. Schweitzer and W. Ziehl, IEEE Trans. Nucl. Sci. **30**, 380 (1983).
[68] M. Valiev, E. J. Bylaska, N. Govind, K. Kowalski, and T. P. A. Straatsma, Comput. Phys. Commun. **181**, 1477 (2010).
[69] M. P. A. Prange, Phys. Rev. B **87**, 115101 (2013).
[70] N. Govind, P. V. Sushko, W. P. Hess, M. Valiev, and K. Kowalski, Chem. Phys. Lett. **470**, 353 (2009).
[71] L. F. Pacios and P. A. Christiansen, J. Chem. Phys. **82**, 2664 (1985).
[72] M. M. Hurley, L. F. Pacios, P. A. Christiansen, R. B. Ross, and W. C. Ermler, J. Chem. Phys. **84**, 6840 (1986).
[73] F. Weigend and R. Ahlrichs, Phys. Chem. Chem. Phys. **7**, 3297 (2005).
[74] J. P. Perdew, K. Burke, and M. Ernzerhof, Phys. Rev. Lett. **77**, 3865 (1996).
[75] J. P. Perdew, M. Ernzerhof, and K. Burke, J. Chem. Phys. **105**, 9982 (1996).
[76] C. Adamo and V. Barone, J. Chem. Phys. **110**, 6158 (1999).
[77] P. Cortona, J. Chem. Phys. **136**, 086101 (2012).
[78] C. A. Guido, E. Bremond, C. Adamo, and P. Cortona, J. Chem. Phys. **138**, 021104 (2013).
[79] F. C. Brown, C. Ghwiller, H. Fujita, A. B. Kunz, W. Scheifley, and N. Carrera, Phys. Rev. B **2**, 2126 (1970).
[80] R. W. G. Wyckoff, *Crystal Structures* (Wiley, New York, 1963).
[81] A. D. Becke, J. Chem. Phys. **98**, 5648 (1993).
[82] A. D. Becke, J. Chem. Phys. **98**, 1372 (1993).
[83] R. J. Le Roy, J. Quant. Spectrosc. Radiat. Transf. **186**, 167 (2017).
[84] R. N. Zare, J. Chem. Phys. **40**, 1934 (1964).
[85] A. Farazdel, M. Dupuis, E. Clementi, and A. Aviram, J. Am. Chem. Soc. **112**, 4206 (1990).